Journal of Earth Science, Vol. 36, No. 4, p. 1605–1622, August 2025 *ISSN 1674-487X*
Printed in China
https://doi.org/10.1007/s12583-025-0160-2

Air-Space-Ground Synergistic Observations for Rapid Post-Seismic Disaster Assessment of 2025 *Ms*6.8 Xigazê Earthquake, Xizang

Jie Dou[1, 2, 3], **Ke Xing**[1], **Lizhe Wang**[*4], **Haixiang Guo**[5], **Dun Wang**[6], **Yigui Peng**[1],
Xinjian Xiang[1], **Dunzhu Ciren**[7], **Songcheng Zhang**[1], **Lele Zhang**[1], **Bo Peng**[1]
1. *Badong National Observation and Research Station of Geohazards*, *China University of Geosciences* (*Wuhan*), *Wuhan* 430074, *China*
2. *National Engineering Research Center of Geographic Information System*, *China University of Geosciences* (*Wuhan*), *Wuhan* 430074, *China*
3. *Key Laboratory of Geological Survey and Evaluation of Ministry of Education*, *China University of Geosciences* (*Wuhan*), *Wuhan* 430074, *China*
4. *School of Computer Science*, *China University of Geosciences* (*Wuhan*), *Wuhan* 430078, *China*
5. *School of Economics and Management*, *China University of Geosciences* (*Wuhan*), *Wuhan* 430078, *China*
6. *School of Earth Sciences*, *China University of Geosciences* (*Wuhan*), *Wuhan* 430074, *China*
7. *Xizang Autonomous Region Water Conservancy and Electric Power Planning*, *Survey and Design Institute*, *Lhasa* 850010, *China*

ABSTRACT: On January 7, 2025, an *Ms*6.8 earthquake struck Dingri County, Xigazê City, in the Xizang Autonomous Region. The epicenter, located near the Shenzha-Dingjie fault zone at the boundary between the Qinghai-Xizang Plateau and the Indian Plate, marked the largest earthquake in the region in recent years. The Shenzha-Dingjie fault zone, situated at the boundary between the Qinghai-Xizang Plateau and the Indian Plate, is a key tectonic feature in the India-Eurasia collision process, exhibiting both thrust and strike-slip faulting. This study analyzed the disaster characteristics induced by the earthquake using Differential Synthetic Aperture Radar Interferometry (D-InSAR) to process Sentinel-1 satellite data and derive pre- and post-earthquake surface deformation information. Additionally, high-resolution optical remote sensing data, UAV (unmanned aerial vehicle) imagery, and airborne LiDAR (light detection and ranging) data were employed to analyze the spatial distribution of the surface rupture zone, with field investigations validating the findings. Key results include: (1) Field verification confirmed that potential landslide hazard points identified via optical image interpretation did not exhibit secondary landslide activity; (2) D-InSAR revealed the co-seismic surface deformation pattern, providing detailed deformation information for the Dingri region; (3) Integration of LiDAR and optical imagery further refined and validated surface rupture characteristics identified by optical-InSAR, indicating a predominantly north-south rupture zone. Additionally, surface fracture features extending in a near east-west direction were observed on the southeast side of the epicenter, accompanied by some infrastructure damage; (4) Surface fracture was most severe in high-intensity seismic areas near the epicenter, with the maximum surface displacement approximately 28 km from the epicenter. The earthquake-induced surface deformation zone spanned approximately 6 km by 46 km, with deformation concentrated primarily on the western side of the Dingmucuo Fault, where maximum subsidence of 0.65 m was detected. On the eastern side, uplift was dominant, reaching a maximum of 0.75 m. This earthquake poses significant threats to local communities and infrastructure, underscoring the urgent need for continued monitoring in affected areas. The findings highlight the effectiveness of multi-source data fusion (space-air-ground based observation) in seismic disaster assessment, offering a methodological framework for rapid post-earthquake disaster response. providing a valuable scientific foundation for mitigating secondary disasters in the region.

---

*Corresponding author: lizhe.wang@foxmail.com

Manuscript received January 20, 2025.
Manuscript accepted January 28, 2025.

Dou Jie, Xing Ke, Wang Lizhe, Guo Haixiang, Wang Dun, Peng Yigui, Xiang Xinjian, Ciren Dunzhu, Zhang Songcheng, Zhang Lele, Peng Bo, 2025. Air-Space-Ground Synergistic Observations for Rapid Post-Seismic Disaster Assessment of 2025 *Ms*6.8 Xigazê Earthquake, Xizang. *Journal of Earth Science*, 36(4): 1605 – 1622. https://doi.org/10.1007/s12583-025-0160-2. http://en.earth-science.net

KEY WORDS: earthquakes, air-space-ground multi-source observations, 2025 Xigazê *Ms*6.8 earthquake, geohazards assessment, surface rupture characterization, post-seismic geohazard monitoring.

0 INTRODUCTION

Understanding earthquake mechanisms and predicting seismic hazards have long been critical research topics in Earth sciences and remain global scientific challenges (Chen et al., 2022b). Despite notable progress made by researchers over the past decades, earthquake disaster prediction continues to pose substantial difficulties. Field investigations are fundamental methods for studying coseismic surface ruptures, providing detailed local geological and seismic rupture information. However, in remote or harsh climate regions, field investigations are often highly restricted and difficult to conduct comprehensively. Overcoming these limitations and exploring more efficient and reliable approaches for pre- and post-earthquake studies have become pressing scientific issues (Xing et al., 2025; Kang et al., 2023; Dou et al., 2020).

Integrated remote sensing technology, with its extensive monitoring coverage, short update cycles, low acquisition costs, and minimal ground restrictions, has shown great potential in large-scale earthquake monitoring, rapid feature description, and co-seismic rupture pattern analysis (Guo et al., 2023). Early earthquake remote sensing studies relied primarily on geomorphic and topographic analysis methods using multispectral remote sensing images. With continuous technological advancements, methods such as GNSS deformation monitoring, InSAR-based inversion, thermal infrared anomaly monitoring, gravity anomaly monitoring, electromagnetic observation, and chemical element monitoring have been increasingly applied (Mei and Wan, 2024; Yang et al., 2024; Wan et al., 2017; Li et al., 2015). These approaches investigate seismic precursors from various perspectives, particularly in inferring fault activity through geomorphic features and improving our understanding of seismic activity through comprehensive remote sensing, topography, stress fields, and field surveys (Kusky et al., 2023; Meng et al., 2023; Ha et al., 2022; Jara-Munoz et al., 2022; Sarma and Sharma, 2018).

Topography and geomorphology are key reflections of deep-seated tectonic activity. Their diverse linear and planar features can be used to identify concealed or semi-concealed active faults (Ngapna et al., 2018; Wang et al., 2017; Wang et al., 2014). Coseismic surface ruptures, as the most direct surface expression of earthquakes, record abundant information on fault activity. Studying the geometry and spatial distribution of surface ruptures helps reveal the mechanisms of earthquake generation and the regional tectonic evolution characteristics (Duman and Emre, 2013). In recent years, the development of high-resolution remote sensing imagery and photogrammetry methods has provided researchers with higher-precision topographic and geomorphic data (You et al., 2023). These advancements have significantly supported the precise identification of post-earthquake surface rupture zone geometries, fault dislocations, and their spatial distribution characteristics (Krüger and Ohrnberger, 2005). It is particularly noteworthy that interpreting topographic and geomorphic features requires avoiding isolated analysis, as these features are not only related to seismic activity but may also be influenced by climatic, geological, hydrological, and other factors. Therefore, comprehensive analysis of multi-source data is essential to ensure the scientific validity and accuracy of research conclusions.

In recent years, the rapid development of high-resolution remote sensing technology, UAV photogrammetry, and airborne LiDAR spatial measurement technologies has made it possible to quickly acquire high-precision topographic and geomorphic data after earthquakes. These technologies provide crucial data for detailed studies of post-earthquake surface deformation and rupture zones (Yu et al., 2025; Dou et al., 2021). By leveraging these technologies, particularly remote sensing imagery data, researchers can conduct in-depth analyses of coseismic displacement, the spatial distribution of surface rupture zones, and their evolutionary processes (Wang et al., 2018; Liu et al., 2013). For example, high-resolution optical satellites such as GF-1 (2 m resolution) and GF-7 (0.8 m resolution) have enabled detailed studies on the characteristics and spatial distribution of surface rupture zones across different earthquake magnitudes (Zhang et al., 2022; Zhou et al., 2015). In the 2021 Madoi *Ms*7.4 earthquake study, UAV optical imagery revealed not only the typical characteristics of post-earthquake surface ruptures but also enabled quantitative measurement of rupture displacement (Chen et al., 2022). The application of these high-resolution remote sensing data has not only facilitated precise mapping of rupture zone geometries but also further elucidated fault activity patterns and earthquake rupture mechanisms.

With the increasing frequency of seismic activity in Xizang and the Qinghai-Xizang Plateau region, Dingri County, located along the critical seismic belt at the junction of the Qinghai-Xizang Plateau and the Indian Plate, has drawn widespread attention from domestic and international scholars for its seismic disaster impacts and characteristics. The *Ms*6.8 earthquake in Dingri County on January 7, 2025, with its epicenter near the Shenzha-Dingjie fault zone, was the largest earthquake to occur in the region in recent years. The surface deformation zone and fault dislocation triggered by this earthquake provide an valuable case for advancing the understanding of earthquake generation mechanisms and disaster impacts in the region.

In this study, we utilized differential synthetic aperture radar interferometry (D-InSAR), high-resolution satellite imagery, UAVs, and LiDAR-based air-space-ground synergistic observations to conduct a detailed analysis of the surface rupture zone of the January 7, 2025, Dingri County earthquake. The spatial distribution characteristics of coseismic deformation, the geometry of ruptures, and fault activity patterns were examined. The integration of multi-source remote sensing technologies provides high-precision, full-coverage post-earthquake surface deformation data, effectively overcoming the limitations of traditional field investigations and low-resolution remote sensing imagery. This approach offers scientific insights for seismic disaster risk assessment, secondary disaster prediction, and post-earthquake recovery and reconstruction efforts.

1 STUDY AREA OVERVIEW

The continuous convergence and collision between the Indian and Eurasian plates during the Cenozoic Era have led to crustal shortening, thickening, and uplift of the Qinghai-Xizang Plateau, which continues to rise at an average rate of approximately 40 mm per year (Pan et al., 2020). The tectonic system of the region includes the major thrust fault systems of the Himalayas, multiple north-south trending graben (rift) structures, and significant east-west striking strike-slip faults, all of which collectively contribute to the uplift of the Qinghai-Xizang Plateau and regional seismic activity (Huang et al., 2024; Zhang and Gong, 2024).

Dingri County, under the jurisdiction of Xigazê City in the Xizang Autonomous Region, is geographically located between 86°20′E and 88°10′E longitude and 28°20′N and 29°10′N latitude (Figure 1). The area belongs to a temperate semi-arid monsoon climate zone on the plateau. The region's climate is characterized by dryness, significant diurnal temperature variations, and low precipitation. These typical plateau climatic conditions have profound impacts on its geological evolution and disaster characteristics. The terrain of the study area is high in the west and low in the east, with complex and diverse landforms, including valleys, low to mid-altitude mountains, high mountains, gorges, and glacial geomorphology. The primary exposed strata in the region include the Proterozoic Nieramu Group (AnZnl) and the Quaternary loose deposits (Q).

The area's neotectonic movement is dominated by extensional tectonics. Particularly in southern Xizang, near north-south trending rift structures have formed, exhibiting significant seismic activity (Bai et al., 2012). The primary active fault near the earthquake's epicenter in the study area is the Dingmucuo Fault, which remained active after the 2015 Nepal earthquake and serves as an important graben system in the southern segment of the Shenzha-Dingjie fault zone (Institute of Geology, China Earthquake Administration, 2025; Zhang et al., 2002). The Shenzha-Dingjie fault zone consists of multiple grabens and horsts, forming a graben-horst structural belt with high seismicity. This zone plays a critical role in accommodating the eastward extrusion and extension of the Xizangan Plateau, contributing to the region's seismicity and presenting significant earthquake hazards due to the accumulation of tectonic stress. Since the Holocene, this region has experienced significant tectonic movements multiple times (Li et al., 2025).

2 METHODOLOGY

2.1 Optical-InSAR Satellite Images for Rapidly Interpreting Epicenter Buffer Zone Disaster Characteristics

Identifying and monitoring earthquake-induced surface deformation is one of the core directions in seismic disaster research (Xu et al., 2019). Traditional monitoring techniques, such as GPS and leveling surveys, are effective in monitoring known landslide disasters within small areas but present significant limitations (Zhu et al., 2017). These methods are often constrained by low spatial resolution, the need for field measurements, and the inability to achieve real-time monitoring. In complex terrains such as mountainous valleys, field investigations are inefficient, costly, and lack sufficient coverage (Mao et al., 2024). Therefore, the use of high-precision Earth observation technologies, particularly those based on multi-platform optical remote sensing, radar remote sensing, and LiDAR technologies, has become a breakthrough approach for monitoring seismic surface deformation.

Optical remote sensing imagery offers broad coverage and high resolution, providing detailed insights into earthquake-related terrain features, geological backgrounds, and underlying substrates (Peng et al., 2017). Such imagery not only aids in identifying large-scale post-earthquake surface deformations but can also be used for retrospective analysis of historical deformations, offering valuable insights for seismic disaster risk assessment. However, optical remote sensing is often hindered by cloud cover and rainfall in many regions, limiting its real-time data acquisition capabilities.

InSAR technology overcomes these limitations by effectively penetrating clouds and acquiring extensive surface deformation information (Lu et al., 2019). Particularly, Sentinel-1 satellite P48 track C-band data, with its wide coverage, is suitable for earthquake monitoring. In this study, SAR imagery was used to obtain pre- and post-earthquake data, which were analyzed using D-InSAR techniques. Terrain phase correction was conducted with the Copernicus 30-meter resolution digital elevation model (DEM), and temporary orbital data from the European Space Agency was employed to eliminate orbital errors, further enhancing data accuracy. During data processing, an adaptive filtering algorithm was applied to suppress noise, and areas with coherence coefficients below 0.3 were masked. The minimum cost flow (MCF) method (Costantini, 1998) was then used for phase unwrapping to accurately reconstruct deformation fields. Finally, after transforming the data into a geographic coordinate system, the coseismic deformation distribution of the Dingri earthquake was obtained.

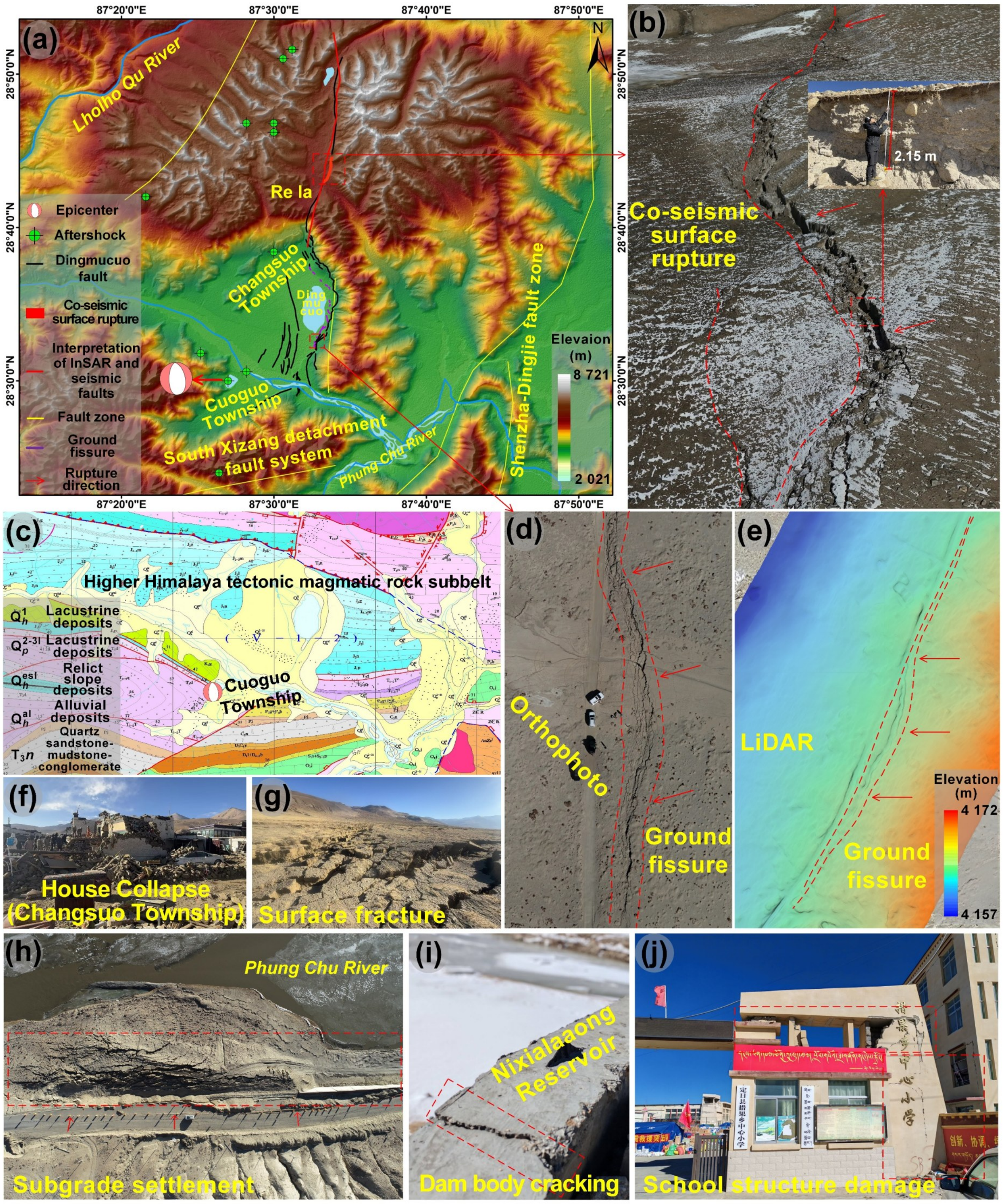

Figure 1. Earthquake area overview map. (a) Earthquake region and fault information; (b) co-seismic surface rupture; (c) geological map; (d) UAV orthophoto image; (e) airborne LiDAR imagery; (f) residential building damage in the seismic area; (g) surface fracture; (h) ground subsidence; (i) dam body cracking; (j) school damage (rupture data from China Earthquake Administration (CEA), aftershock data from China Seismological Network (CSN)).

2.2 LiDAR-Optical UAV High-Precision Topographic Survey for Surface Rupture Characterization

Based on rapid interpretation results from optical satellite and InSAR data, this study employed a combination of LiDAR and optical UAV remote sensing technologies to conduct precise analyses of post-earthquake surface deformations. First, high-resolution optical satellite imagery was used for macro-level surface interpretation, enabling the identification of significant post-earthquake changes such as tensile cracks, folds, and faults within large-scale geological structures. These images provided critical clues for the initial identification of major deformation zones in the earthquake-affected region. Subsequently, InSAR technology was used to obtain surface deformation information, detecting subtle displacements and revealing the direction and rate of surface movement post-earthquake, thereby inferring the activity range and deformation characteristics of the source zone.

On this basis, high-resolution orthophotos (digital orthophoto map, DOM) of the post-earthquake region were obtained using UAV photogrammetry. These images captured surface changes on a microscopic scale, particularly small-scale surface cracks, collapses, and other detailed features. The maximum resolution of the DOM can reach 1.74 cm. Airborne LiDAR technology, through laser scanning, acquired high-precision 3D point cloud data, not only providing accurate surface elevation measurements but also clearly delineating crack directions, surface rupture dislocation orientations, and other surface rupture details, further supplementing optical satellite and InSAR data.

LiDAR and UAV imagery exhibit significant advantages in providing more detailed topographic data than satellite imagery and InSAR, enabling precise measurements of post-earthquake surface deformation and quantification of crack sizes, dislocation directions, and magnitudes (Zhang et al., 2024; Xu, 2020). By integrating optical satellite, InSAR, UAV imagery, and LiDAR data, comprehensive analyses of surface rupture phenomena can be achieved, encompassing macro- to micro-scale precise descriptions. This multi-source data integration method not only accurately characterizes earthquake-induced surface rupture features, dislocation directions, and post-earthquake evolutionary processes but also delineates earthquake impact ranges, aids in source zone activity analysis, and assesses aftershock impacts on surface rupture aggravation. This approach provides scientific support for post-disaster recovery and disaster warning and supports subsequent earthquake monitoring and risk assessments.

2.3 Analysis of Surface Rupture Indicators Based on Seismic Intensity Range and Aftershock Distribution

When analyzing surface rupture indicators induced by earthquakes, the seismic intensity distribution and the spatial-temporal evolution of aftershock sequences are crucial factors (Wang et al., 2023). Delineating seismic intensity zones provides insight into the earthquake's impact strength on the surface, while the spatial distribution and subsequent activities of aftershocks offer indications of the continued evolution of surface ruptures post-earthquake. The greater the intensity, the more severe the surface damage and topographic deformation. Generally, in high-intensity zones (IX degree and above) near the epicenter, surface ruptures manifest as significant fault dislocations, tensile cracks, and compressional features, often accompanied by substantial topographic deformation, such as vertical fault displacement and surface crack propagation (Wu et al., 2015). Meanwhile, low-intensity zones may exhibit minor cracks or slight landslide phenomena, which gradually evolve under the continuous effects of aftershocks.

Aftershocks are extensions of seismic activity following the mainshock, and their distribution and intensity are usually closely related to the mainshock's fault structures and crack propagation paths (Deng et al., 2014). By analyzing the spatial-temporal characteristics of aftershocks, the primary active zones of aftershocks and their further impacts on surface fractures can be identified. Especially in the later stages of an earthquake, aftershock activities often extend along the mainshock fault and induce secondary fractures or exacerbate existing crack propagation in adjacent areas. By analyzing the spatial trajectories of aftershocks and combining them with seismic intensity ranges, the locations of surface rupture zones can be further pinpointed and their potential expansion directions predicted.

3 RESULTS

3.1 Interpretation of Optical-InSAR Satellite Data

The epicenter is located in the southern part of the Yarlung Zangbo River Basin on the Qinghai-Xizang Plateau. This region not only faces the threat of destructive earthquakes to human lives and property but also poses significant risks to the stability of slopes in surrounding watersheds and critical infrastructure such as hydropower stations. While traditional GPS point-based monitoring techniques provide some surface displacement information, their spatial coverage and monitoring frequency are limited, making it challenging to comprehensively and dynamically reflect large-scale surface deformations in the region. Therefore, this study integrates optical imagery, InSAR technology, and field investigations to accurately identify and monitor earthquake-induced surface deformation, aiming to comprehensively understand the distribution of deformation characteristics in the affected area and assess the potential development of secondary disasters.

The severity of earthquake damage is not only closely related to the earthquake magnitude but also influenced by factors such as focal depth, geological structure, and building quality. Studies indicate that earthquakes with magnitudes of 6.0 or higher can cause severe damage to buildings and infrastructure within a 100 km radius of the epicenter, while areas beyond 300 km are typically unaffected unless under specific geological conditions (Chen, 2017). However, the actual impact of the earthquake requires a comprehensive scientific evaluation and determination, which should clarify the geological context, aftershock distribution, source mechanism, and strong-motion records, while also integrating field investigations.

To quantitatively assess the impact range of the earthquake on the terrain, this study constructed a post-earthquake impact model based on the distribution of river systems in the Xizang region (Figure 2). The model integrates aftershock distribution and epicenter location, statistically analyzing the effects at different buffer zones from the epicenter to assess the energy transmission characteristics of the earthquake. In Figure 2, the blue

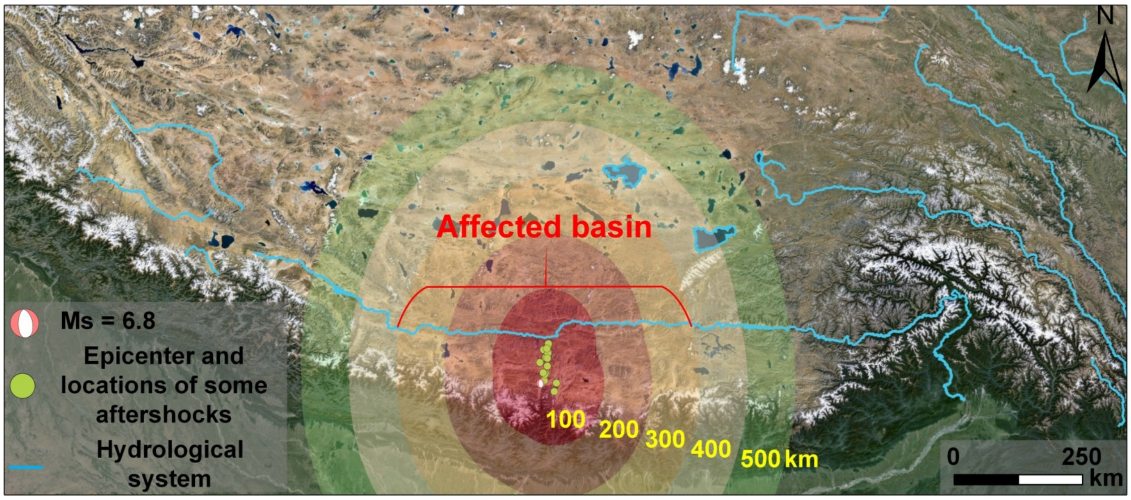

Figure 2. Schematic of the earthquake epicentre buffer zone.

curves represent seasonal rivers in the Yarlung Zangbo River Valley, while the buffer zones illustrate the varying intensity impact ranges extending outward from the epicenter. The study results indicate:

(1) Red zone (within 100 km): Intensity reaches VI or higher. The epicentral area experiences significant destruction, with notable surface deformation and a high likelihood of large-scale secondary disasters.

(2) Orange to yellow zones (200–300 km): Intensity ranges from III to V, with substantial impacts and possible secondary disasters such as avalanches and debris flows.

(3) Light yellow to green zones (400–500 km): Intensity ranges from I to II. Although seismic sensations are weaker, secondary disasters may still occur.

(4) Beyond the green zone: Minimal seismic perception, with limited earthquake impact.

Special attention should be paid to the Yarlung Zangbo River Valley and its seasonal tributaries, particularly areas within the 0–300 km buffer zones. These regions may face threats from avalanches, glacial lake outbursts, and debris flows post-earthquake. Additionally, a series of NS striking graben systems associated with tectonic activity may pose significant risks to local infrastructure and ecosystems.

Through comparative analysis of historical satellite images within the seismic area, potential landslide hazard sites were identified (Figure 3). Results show that most hazard sites are located in valley regions with steep terrain, with slopes ranging from 30° to 60°. The boundaries of these hazard sites often align with terrain boundaries. The slope materials mainly consist of weathered debris, gravel, and clay layers, with uneven thickness in the weathered cover. In some hazard sites, the rear deposits are relatively thin, exposing significant bedrock, while the central and frontal deposit layers gradually thicken, with some local accumulations reaching tens of meters. In the southern part of the hazard sites, glacial deposits were observed at the mountain tops (Figure 3III). The slope morphology is mainly elliptical or elongated tongue-shaped, with length-to-width ratios ranging from 1 : 1 to 1 : 4 and lengths reaching 100 to 500 meters. Although these hazard sites are far from residential areas, they pose significant threats to downstream rivers and roads. Field investigations revealed that most hazard sites are ancient landslide zones (Figure 3II) that were not affected by the recent earthquake and showed no new signs of sliding. This finding suggests that the historical landslides in this region are relatively stable, and the likelihood of large-scale sliding in the short term is low. However, continuous monitoring is necessary to prevent potential secondary disasters.

After the earthquake, micro-geomorphic features such as fault steps, strike cracks, shadows, and surface facility damages often appeared along fault directions. The surface deformation caused by the earthquake exhibited diverse forms, and not all earthquake rupture features could be fully represented. Figure 4 shows a comparative analysis of pre- and post-earthquake images in typical surface rupture zones. By comparing changes in remote sensing images before and after the earthquake, results indicate that no significant surface faults, cracks, or deposit layer slides were observed in historical hazard areas, suggesting limited impact of this earthquake on existing landslide areas. The optical image data used in this study were sourced from Google Earth and the Chinese Gaofen-1 satellite (GF-1). The multispectral color images obtained from GF-1 (including blue, green, red, and near-infrared bands) significantly improved the recognition of target features. As shown in Figure 4, the surface features of the eastern coast of Dingmucuo before the earthquake were relatively flat. Post-earthquake images revealed multiple east-west-oriented crustal ruptures and dislocation features in this area, forming folds and tensile cracks. The rupture gaps were linearly distributed along the eastern coast, with rupture lengths of approximately 11 kilometers. The identification of these rupture features provides important data support for further research on the mechanisms of surface ruptures and fault activities in this region.

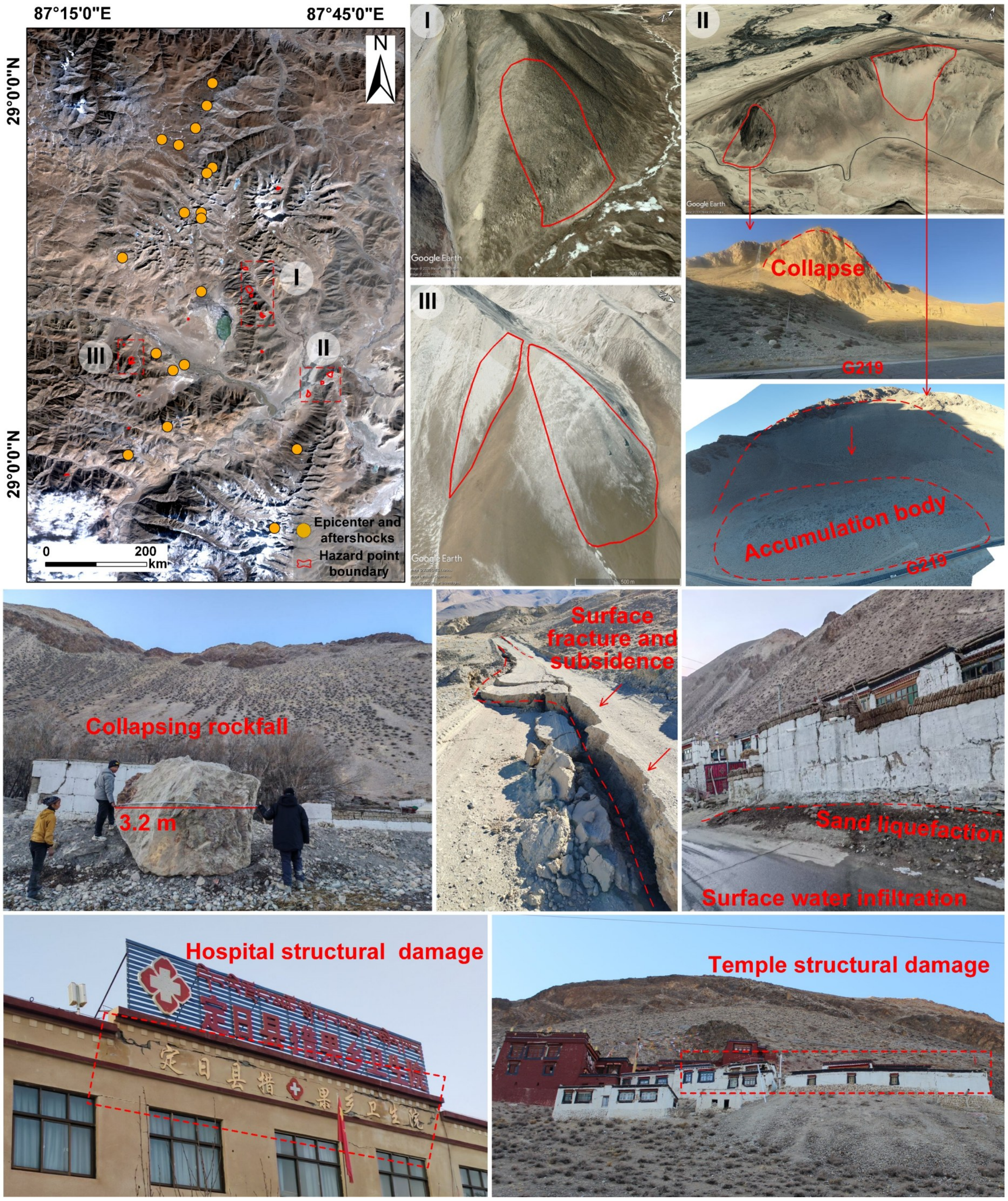

Figure 3. Distribution of satellite interpreted slope hazard sites in the earthquake epicentre area and field investigation map.

Based on remote sensing image analysis and integrated with InSAR technology, this study further conducted quantitative analysis of coseismic surface deformation. Figure 5a shows the coseismic differential interferogram of the Dingri earthquake derived from Sentinel-1 descending track P121 data. The interferogram reveals a butterfly-shaped pattern symmetrically distributed along the Dingmucuo fault with an east-west orientation. The eastern side of the interferogram shows good continuity, while the western side exhibits high surface deformation gradients due to fault rupture propagation effects, resulting in localized decorrelation, reflecting strong seismic deformation characteristics.

Figure 5b presents the quantitative analysis results based on the coseismic deformation data, indicating that the western side of the fault primarily experienced line-of-sight (LOS) subsidence with a maximum value of 0.65 m, whereas the eastern side predominantly experienced uplift with a maximum value of 0.75 m. Further analysis reveals that the deformation impact range on the western side is significantly larger than that on the eastern side, demonstrating the asymmetry of fault activity.

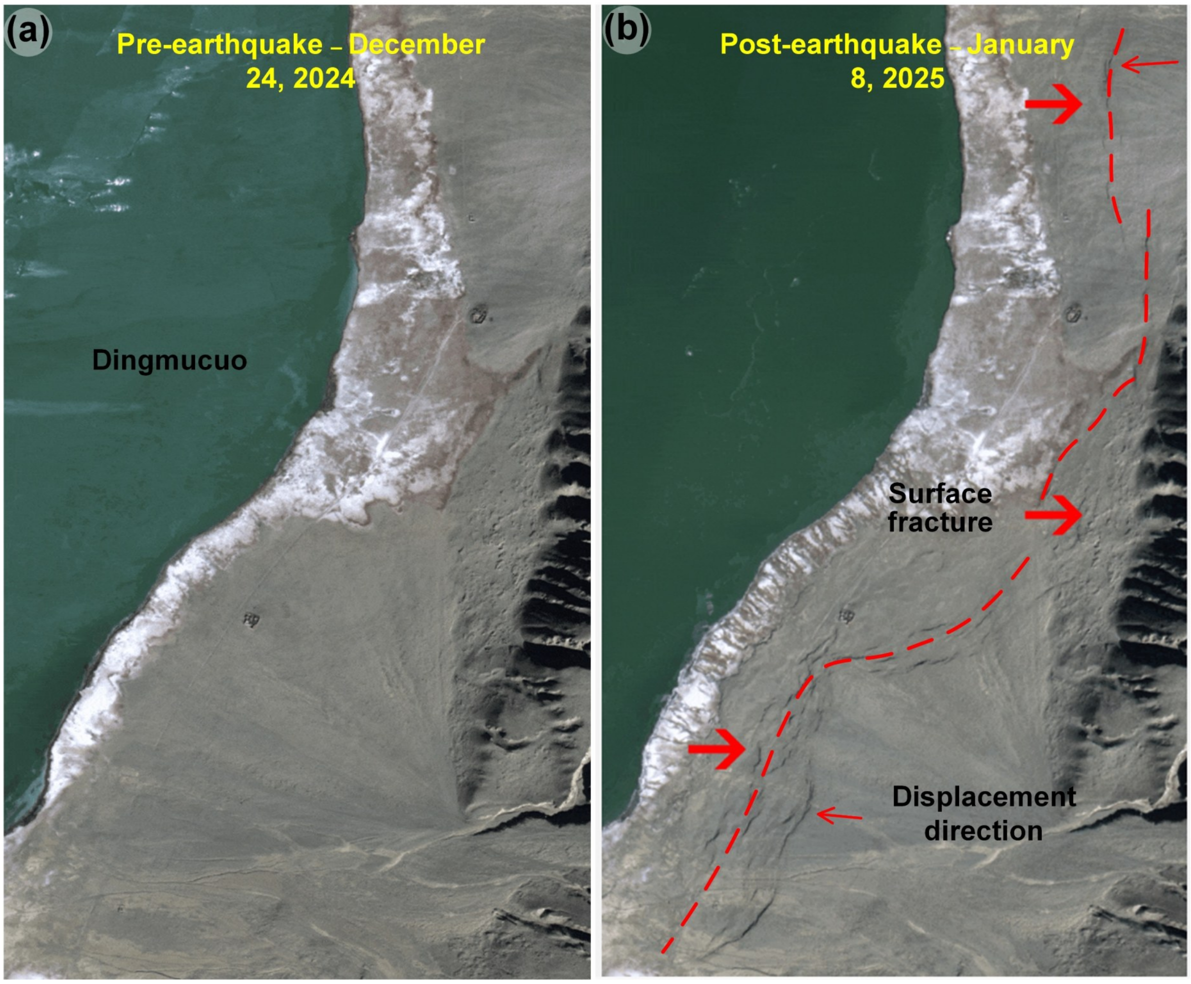

Figure 4. Gaofen-1 satellite acquires pre- and post-earthquake images of the surface of the east coast of Dingmucuo, the area at the epicentre of the earthquake (source: China Land Observation Satellite Data Centre).

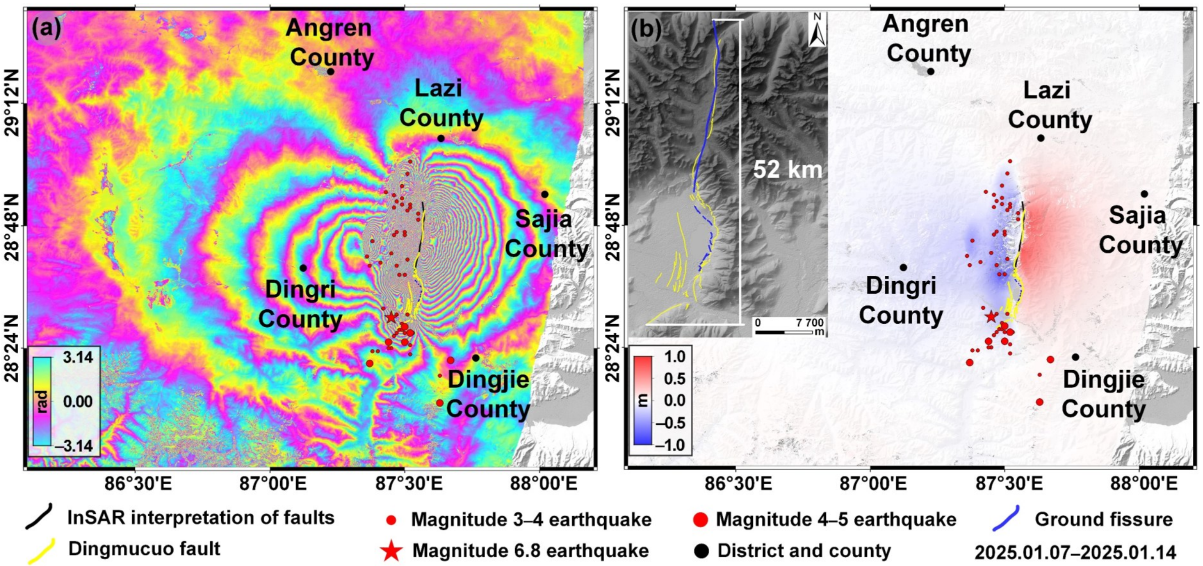

Figure 5. Sentinel-1 D-InSAR results: (a) differential interferogram; (b) LOS to deformation map.

Combining the spatial distribution characteristics of the coseismic deformation field and the regional geological background, this study preliminarily identifies the Dingmucuo fault as the seismogenic fault for this earthquake. The significant activity of this fault and the east-west surface deformation differences indicate its dominant role in this earthquake, providing important evidence for subsequent studies on fault dynamic mechanisms.

3.2 LiDAR-Optical UAV Analysis

The integrated results of LiDAR and optical imagery reveal clear continuity and regularity in surface ruptures (Figure 6). Along the Dingmucuo fault, the surface rupture generally extends in a north-south direction. According to the DOM and DEM images captured by UAVs, the rupture fissures on the eastern side of Dingmucuo exhibit linear distribution, with a length of approximately 10 kilometers, spanning from the mountain base to the shores of Dingmucuo Lake, covering a wide area. The fissures show varying degrees of tensile characteristics and are accompanied by localized surface uplift.

East-west cross-sectional analysis indicates that the rupture along the lakeshore direction experienced significant dislocation, displaying near east-west tensile characteristics. This dislocation is likely due to the interaction between lacustrine deposits and colluvial materials covering the lakeshore area and the deeper stratigraphic layers, leading to the extension of deep crustal faults to the surface and causing significant displacement.

The crustal ruptures and east-west dislocations induced by the earthquake may be closely related to the gradual attenuation of stress propagation and the buffering effect of weak strata against stress (Lu et al., 2024). Under the influence of the mainshock, the surface experienced compressional and extensional effects, forming clearly visible rupture features. Additionally, a surface rupture zone extending in an approximately east-west direction was observed about 3.5 kilometers southeast of the epicenter, accompanied by dislocation pointing toward the Phung Chu River. The continuous occurrence of aftershocks may further exacerbate surface rupture phenomena, causing fault-induced fractures driven by deep stress to expand under the influence of aftershocks, thereby increasing the depth and width of surface ruptures to varying degrees.

By combining high-resolution LiDAR and optical imagery from UAVs, this study achieved rapid acquisition and detailed identification of the spatial distribution characteristics of surface ruptures. The in-depth analysis of the overall orientation and distribution of surface ruptures provides critical technical support for post-earthquake disaster assessment and secondary disaster monitoring, as well as scientific guidance for delineating priority areas for emergency response after the earthquake.

Detailed surveying and mapping of surface deformation along the southeastern to northeastern shores of Dingmucuo (Figure 7a) revealed fault distribution characteristics. Results indicate that the area is primarily characterized by normal faulting, accompanied by complex deformation patterns of dextral and sinistral ground deformation. For significant surface fractures in deformation regions, tensile depth measurements and profile analyses were conducted. The analysis revealed a maximum shear displacement depth of approximately 1 meter, while localized sliding and compressional bulging reached depths of about 0.3 m (Figure 7b).

Parallel profile deformation analyses showed irregular surface fracture patterns, reflecting the complexity of seismic activity in the area, which may be influenced by overlapping fault zones. Local deformation features, such as bending, cracking, and localized uplift, indicate spatial variations in stress release patterns, further revealing the intricate deformation mechanisms within the fault zone.

After the *Ms*6.8 earthquake on January 7, 2025, aftershock activity continued to propagate along a north-south orientation, with the *Ms*5.0 aftershock on January 13, 2025, being particularly notable. Comparative analysis of pre- and post-aftershock UAV orthophotos (Figure 8) revealed increased tensile depths in surface fractures following the aftershock. Original compressional bulging features became more flattened, and the width of some tensile fissures expanded. These observations suggest that aftershocks may further exacerbate surface fracture phenomena, accelerating stress release and fault activity expansion.

Supported by airborne LiDAR technology, surface deformation features were captured with greater precision. LiDAR data clearly revealed the texture characteristics of surface fractures, providing critical information on their spatial extent and orientation, which aids in tracking the morphological evolution of surface fractures (Figure 9). Additionally, the DEM constructed from LiDAR data provided essential support for analyzing elevation changes along fault zones on a regional scale. This data not only enables precise evaluation of the spatial distribution characteristics of fault-induced fractures but also offers a scientific basis for further studies on regional tectonic deformation and its implications.

In summary, the combined analysis of UAV orthophotos and LiDAR data provides a more comprehensive understanding of the impact of aftershocks on surface ruptures, enhancing knowledge of regional tectonic activity and offering reliable data support for subsequent disaster assessment and mitigation efforts.

Approximately 11 km north of Changsuo Township, a coseismic surface rupture zone approximately 4 km in length was identified (Figure 10a). This rupture zone extends southward, causing significant damage to the dam structure of the Nixialaang Reservoir, with crack depths reaching 1.6 meters (Figure 10e). Further south along the rupture zone, the fault extends into the frozen area of a lake, leading to ice surface fractures and localized dislocations. As temperatures rise, the melting ice surface may result in seepage, further compromising the stability of the reservoir dam. This surface rupture poses a substantial risk to the safety of regional engineering infrastructure, particularly as cracks in the reservoir dam could threaten downstream water security (Figure 10d). Therefore, it is essential to conduct continuous post-earthquake monitoring of the reservoir dam and the surrounding hydrological environment to assess dynamic

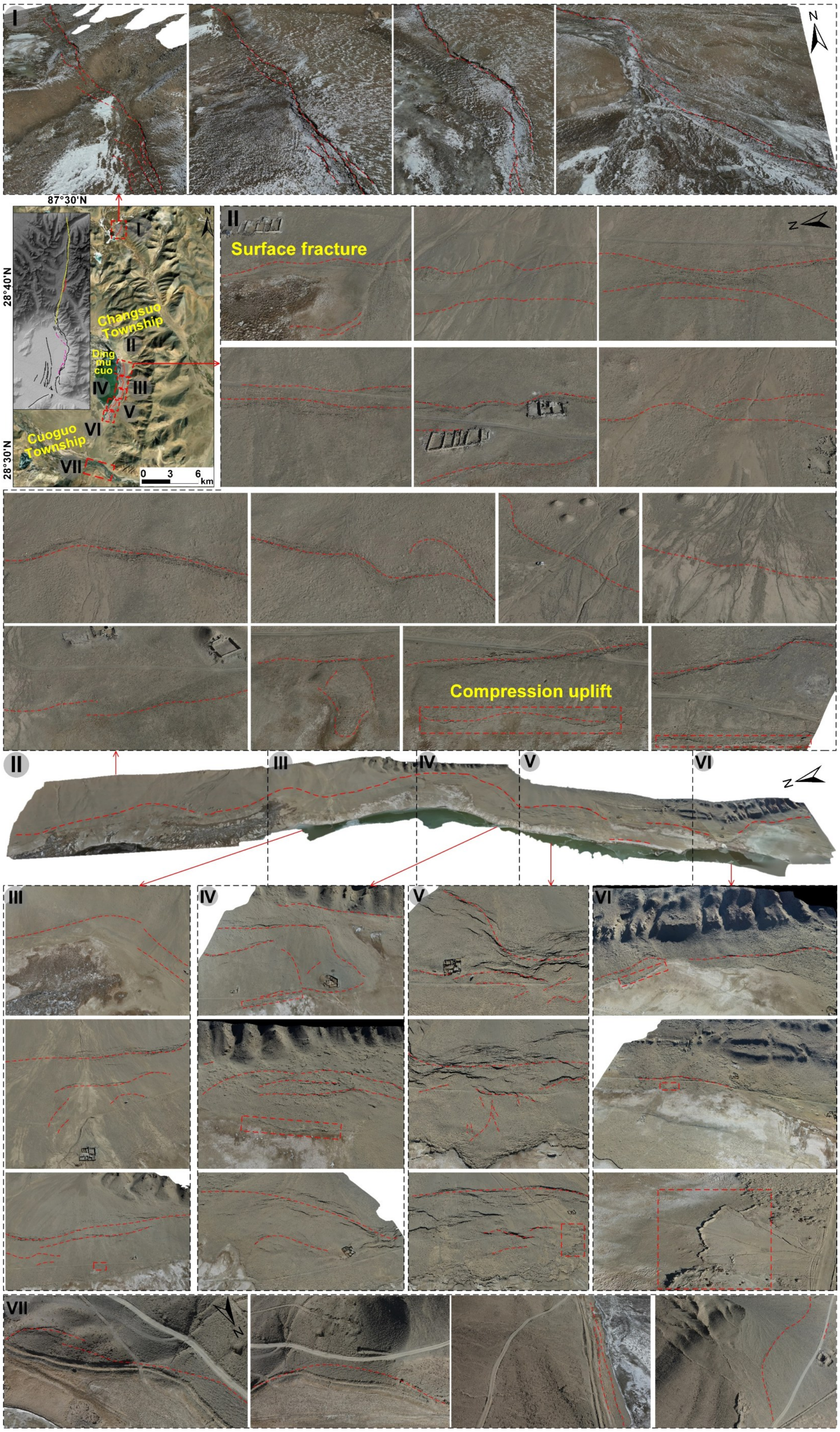

Figure 6. North-south trending surface rupture drone positives.

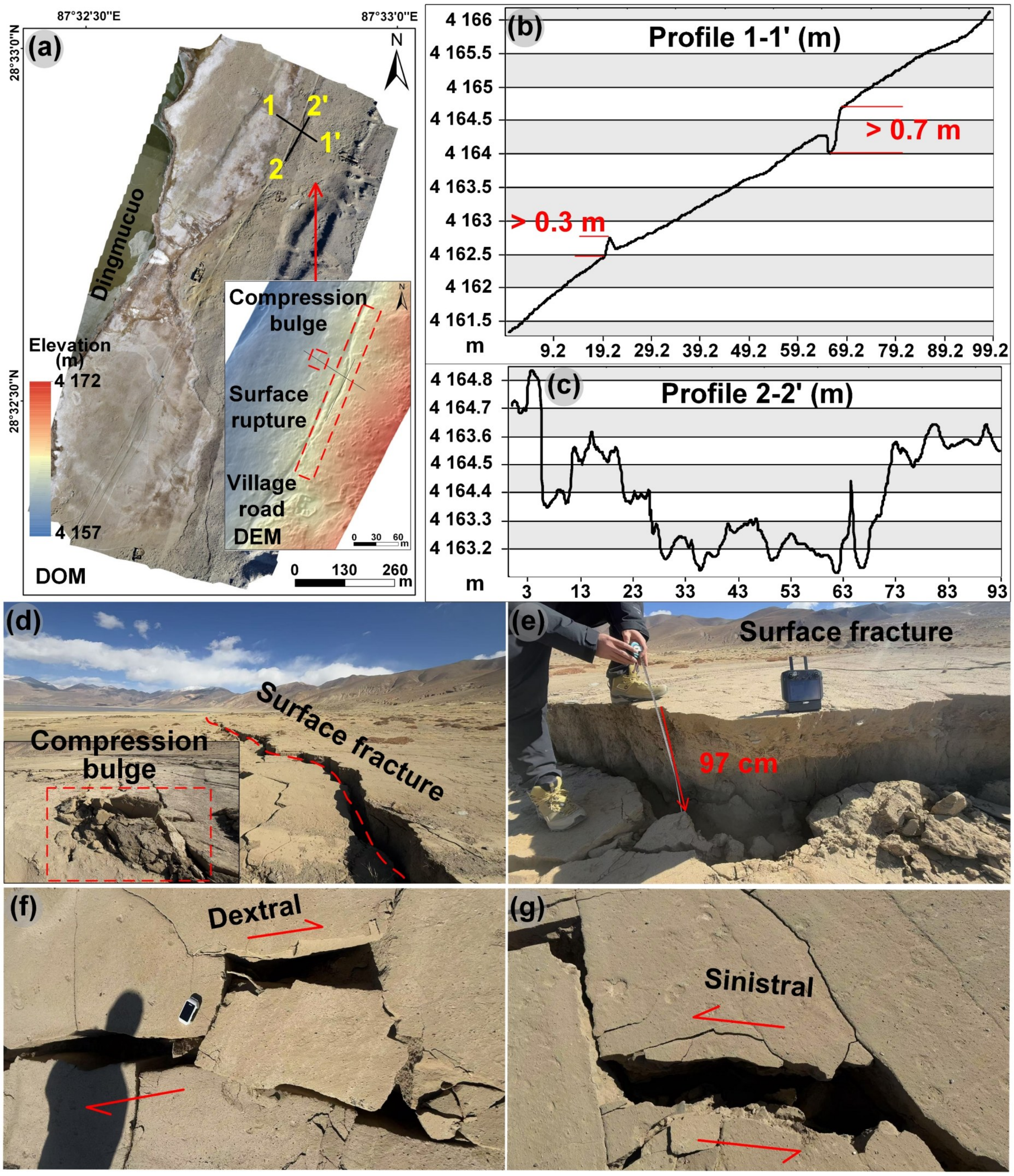

Figure 7. Surface fracture measurements and profiles on the south-east side of the Dingmucuo.

changes in the cracks and prevent secondary disasters caused by seepage.

3.3 Surface Rupture Trend Analysis

In the epicentral region of the *Ms*6.8 earthquake in Dingri County, the surface rupture zones predominantly follow a north-south orientation, consistent with the direction of the Dingmucuo fault. The morphology of surface ruptures is characterized primarily by cracks and dislocations, with significant surface ruptures concentrated in the IX intensity zone (Figure 11). The surface deformation characteristics closest to the epicenter are relatively small, while the largest displacement occurs approximately 11 km north of Changsuo Township, with a range of 2 to 4 meters, about 28 km from the epicenter. Along the eastern shore of Dingmucuo Lake, various deformation phenomena, including imbricate surface fracture, compressional features, and graben formation, demonstrate the complex nature of surface deformation.

Aftershocks continued to distribute along the north-south axis and further intensified the expansion of surface ruptures. Field observations and remote sensing image analyses indicate that aftershock activity has led to increased widths and depths of surface cracks, with dislo-

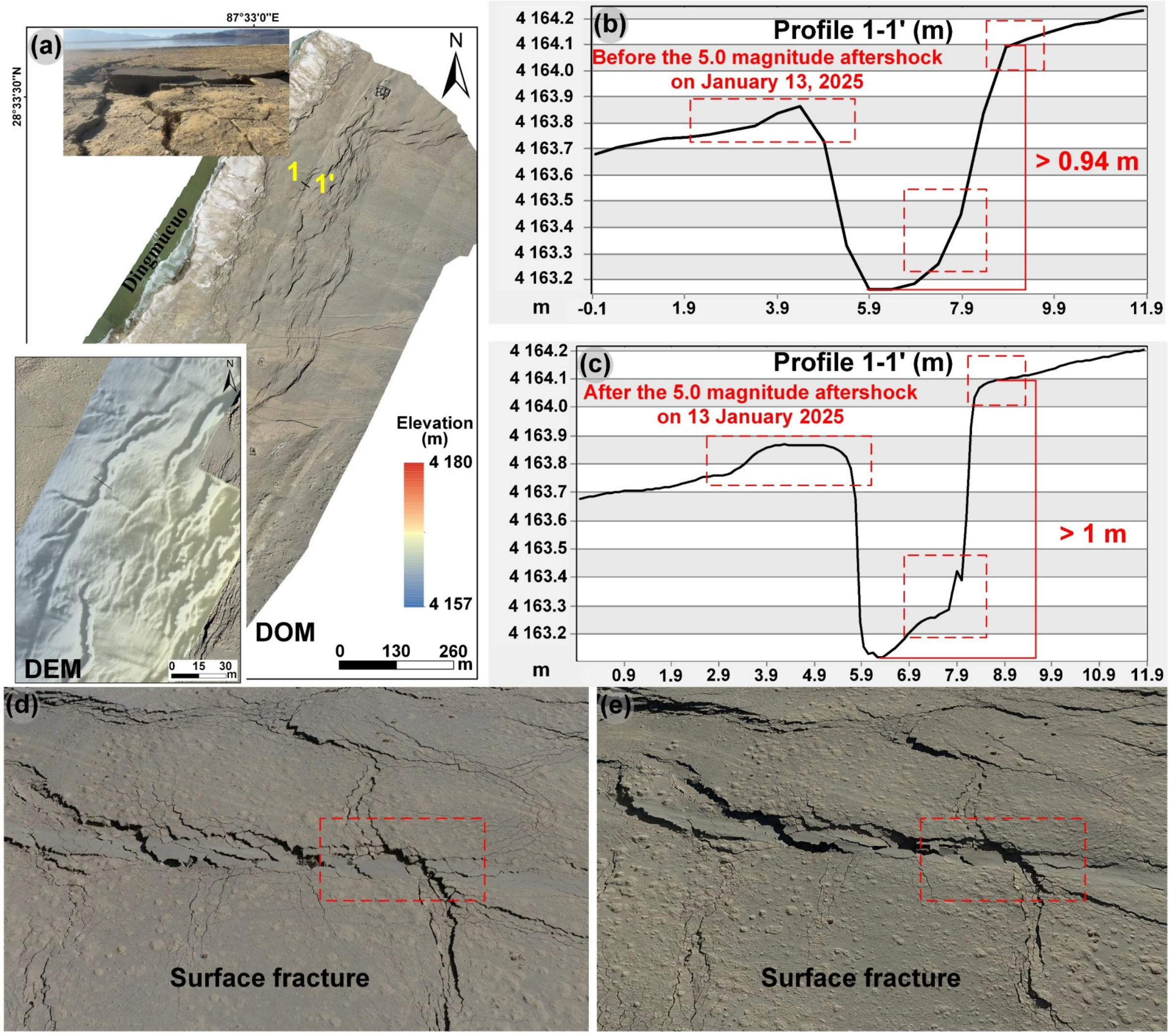

Figure 8. Comparison of surface fracture before and after the aftershock.

cation features becoming more pronounced in localized areas. This suggests that aftershocks may accelerate the evolution of surface fractures, posing greater risks to regional geological stability and infrastructure safety. Strengthening post-earthquake aftershock monitoring, combined with high-precision remote sensing technology, ground observations, and numerical simulations, can provide a more comprehensive assessment of the spatio-temporal evolution of surface fractures. Such efforts will offer critical scientific support for earthquake disaster prevention and infrastructure safety assurance.

4 DISCUSSION

This study identified potential secondary disaster hazard points based on multi-source remote sensing data from air-space-ground integrated systems. However, the evolution of these hazards and their relationship with post-earthquake environmental changes require further discussion. A key question is whether the risks of secondary disasters in specific areas significantly increase due to terrain conditions, climate change, or infrastructure vulnerabilities. Future research should integrate geological, meteorological, and human activity factors to evaluate the evolution trends of these hazard points and develop appropriate mitigation strategies.

The impact of aftershocks is a critical point of discussion in this earthquake disaster study. How can the influence of aftershocks on the depth, width, and evolution process of surface fractures be quantitatively assessed? Can historical earthquake data, combined with numerical simulations and machine learning methods, be used to predict the impact range and rupture expansion trends of aftershocks in specific areas? Addressing these questions will improve the scientific prediction capabilities for aftershock disaster risks.

Furthermore, while this study provides rapid response techniques for post-earthquake disaster assessment, integrating these techniques with post-disaster recovery efforts to form more forward-looking and comprehensive disaster prevention strategies remains an area for exploration. Future work should focus on real-time integration and AI-driven analysis of multi-source data, promoting deeper integration of remote sensing, ground monitoring, and disaster management to enhance the ef-

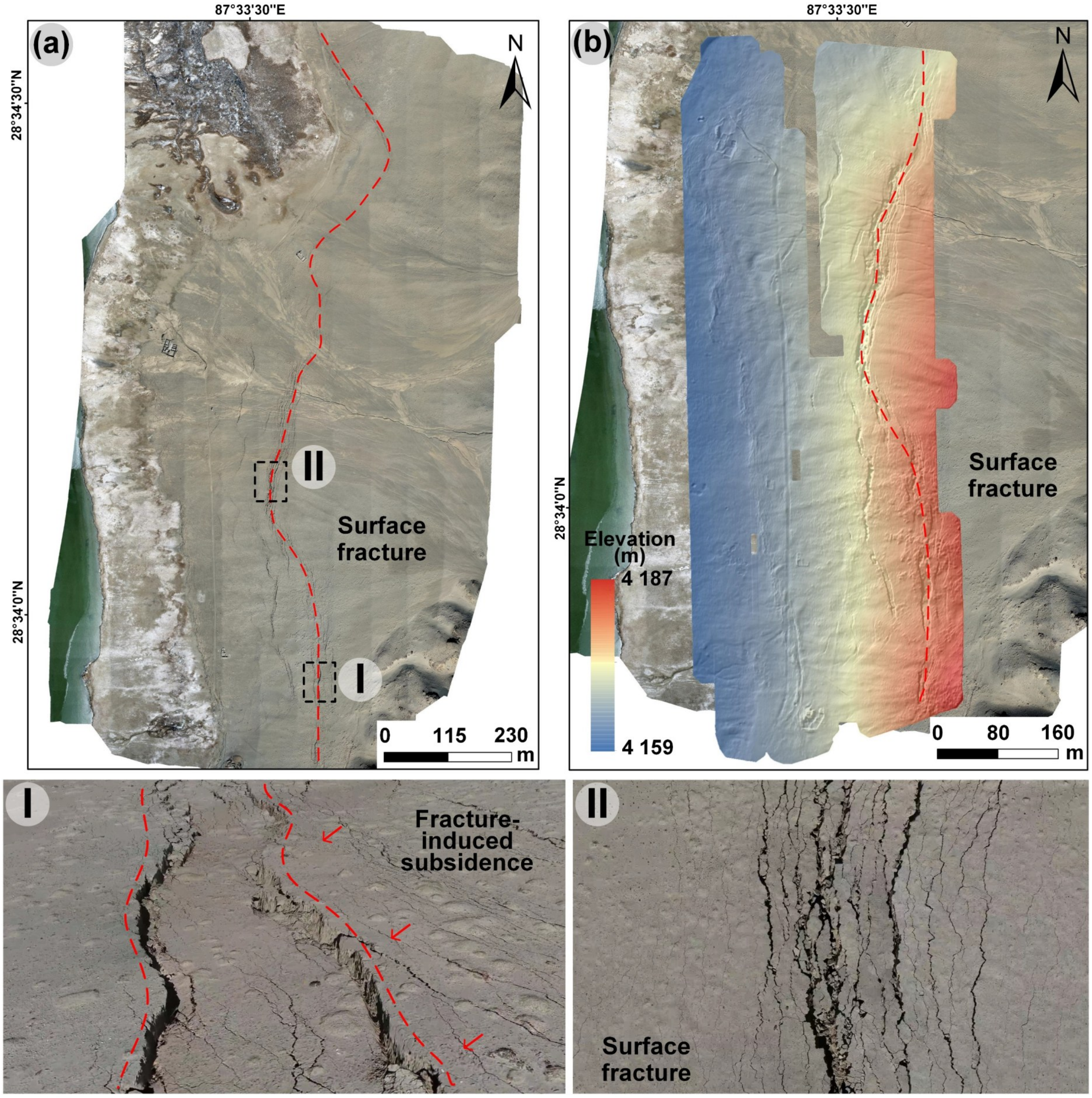

Figure 9. Orthophoto imaging and airborne LiDAR surface breakdown demonstration.

ficiency and scientific accuracy of post-earthquake emergency response (Figure 12).

5 CONCLUSIONS

In response to the *Ms*6.8 earthquake that struck Dingri County, Xizang, on January 7, 2025, this study proposed a post-earthquake rapid response mechanism utilizing multi-source remote sensing technologies. The Dingmucuo fault is part of an east-west extension of the regional tectonic belt associated with the collision, and the seismic hazard is not limited to this fault/rift, but rather extends across the entire area associated with all these faults. First, potential secondary disaster hazards and surface deformation signs were identified through comparative analysis of optical satellite imagery. Subsequently, InSAR technology was applied to analyze surface deformation in the seismic area, identifying deformation zones related to fault activity. By integrating UAV orthophotos and LiDAR technology, detailed topographic data of the seismic area were obtained to analyze the spatial distribution patterns and elevation changes of surface deformation, as well as the evolution trends of surface fractures before and after aftershocks. These findings provide critical scientific insights for post-earthquake disaster assessment and prevention. The main conclusions are as follows:

(1) Identification of post-earthquake secondary hazards and surface ruptures: By combining optical satellite imagery and InSAR technology, potential secondary disaster hazards were identified, and a north-south-oriented coseismic surface rupture zone was detected. The rapid delineation of the epicentral buffer zone, coupled with remote sensing interpretation, provided valuable support for detailed post-disaster investigations and

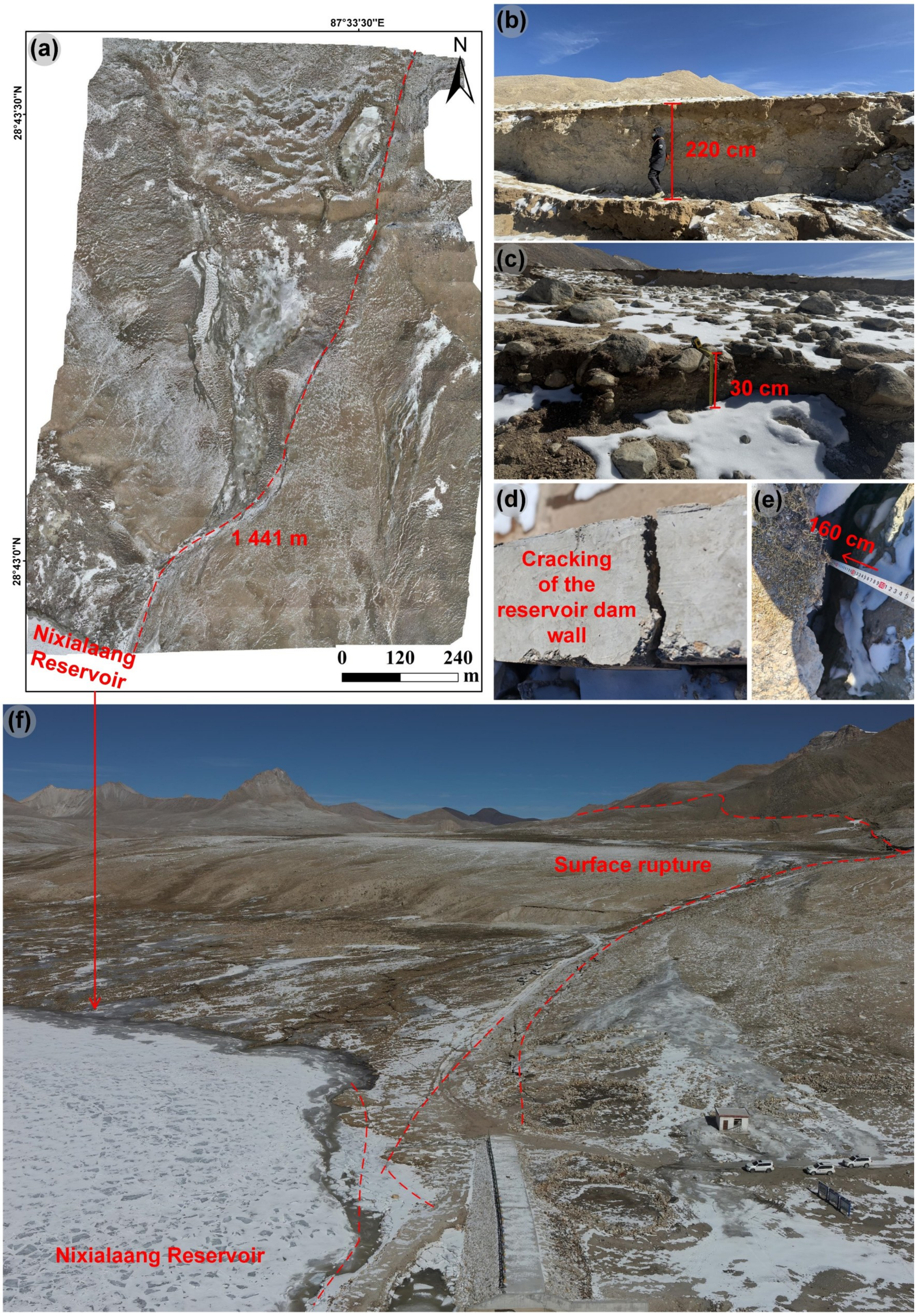

Figure 10. Map of co-seismic surface rupture and damage to reservoir facilities on the north side of Changsuo Township.

surface rupture characterization.

(2) Detailed extraction and analysis of surface deformation features: The integration of high-resolution UAV, LiDAR, and optical imagery enabled precise extraction of surface deformation patterns. The analysis revealed new surface fractures in the southeastern part of the epicenter, contributing critical data for tectonic analysis and validating optical-InSAR remote sensing interpretations.

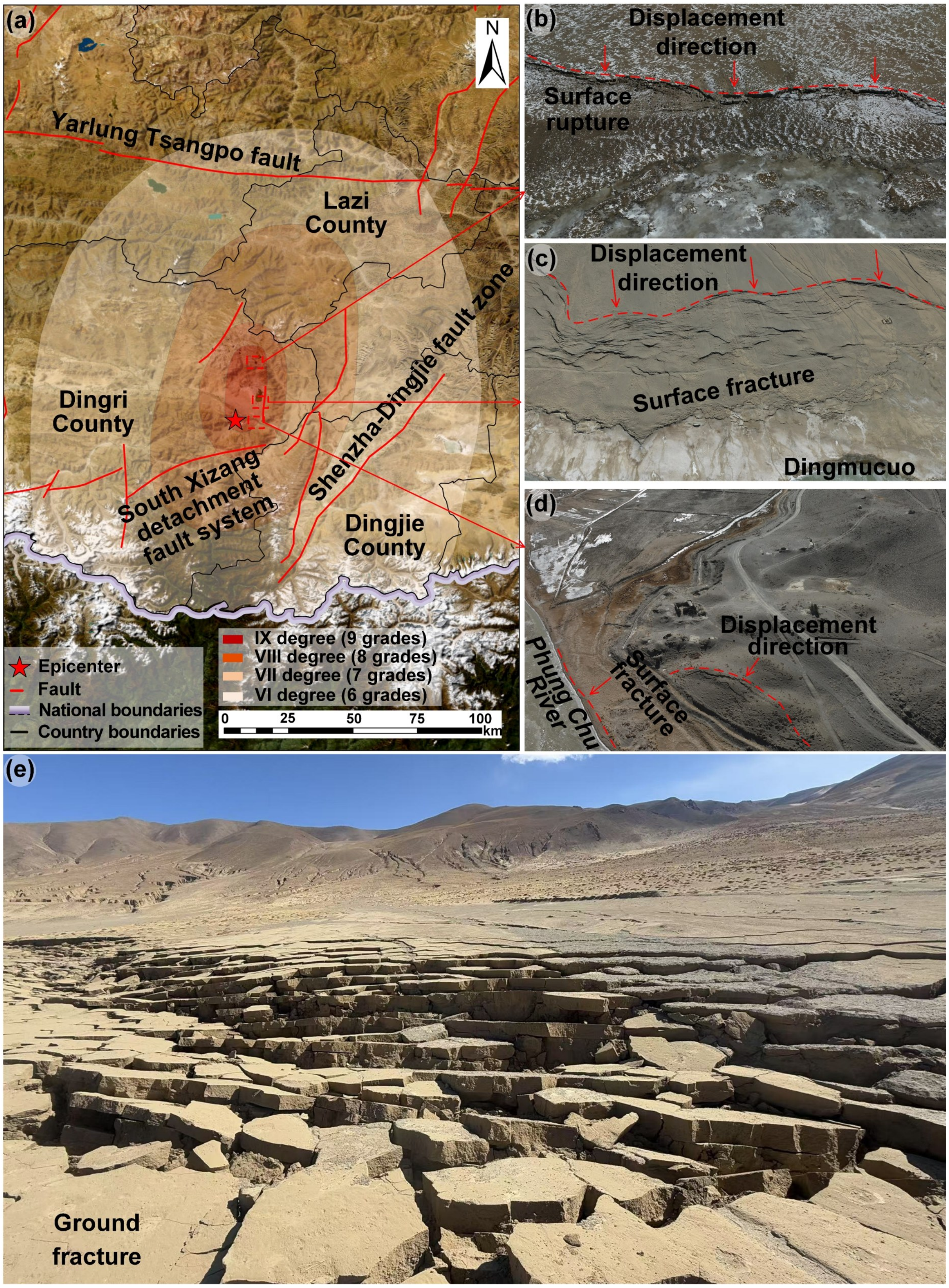

Figure 11. Seismic intensity map distribution and surface rupture (seismic intensity from China Earthquake Administration).

(3) Assessment of aftershock impact on surface fractures: Combining existing seismic intensity distribution with the spatial patterns of aftershock activity, surface rupture phenomena were most severe within the IX intensity zone, with diminishing effects observed in lower intensity zones. Multi-source remote sensing data integration further quantified the progressive impact of aftershocks on surface fractures, providing insights into their

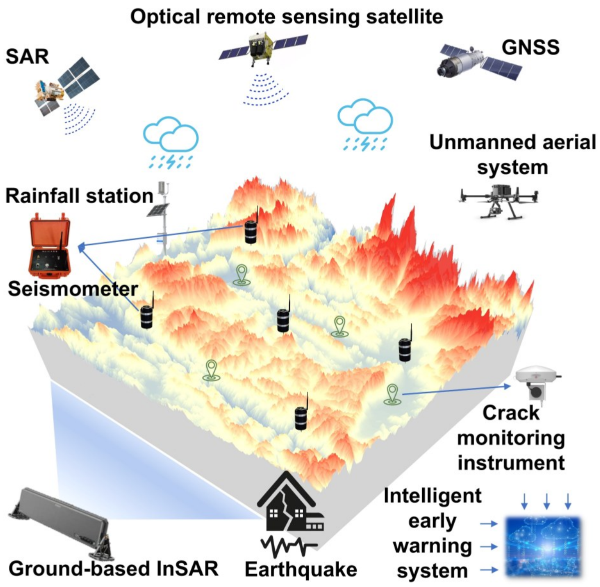

Figure 12. Air-space-ground intelligent monitoring and early warning system.

potential exacerbation over time.

This study presents a scalable framework for monitoring post-earthquake surface deformation and assessing secondary disasters through multi-source remote sensing data. The demonstrated ability to rapidly map deformation zones provides a blueprint for future disaster response strategies. Moving forward, integrating AI-driven automation in damage assessment and real-time deformation tracking could further enhance the resilience of earthquake-prone regions, enabling faster and more precise disaster response efforts.

ACKNOWLEDGMENTS

This study was supported by the National Natural Science Foundation of China (No. 42477170), the Major Project of the National Natural Science Foundation of China (No. 42090054), the Research Fund Program of Hubei Key Laboratory of Resources and Eco-Environment Geology (No. HBREGKFJJ-202411), the Major Project of the National Natural Science Foundation of China (No. 42090054) and Innovative Group Project of Natural Science Foundation of Hubei Province (No. 2024AFA015). The final publication is available at Springer via https://doi.org/10.1007/s12583-025-0160-2.

Conflict of Interest

The authors declare that they have no conflict of interest.

REFERENCES CITED

Bai, Y., Zhang, S. J., Dong, Y. G., et al., 2012. Gravity Field Characteristics and Fault Structures in the Dingri-Muztagh Peak Area, Qinghai-Tibet Plateau. *Geological Review*, 58(2): 237–249. https://doi.org/10.16509/j.georeview.2012.02.016 (in Chinese with English Abstract)

Chen, G. H., Li, Z. W., Xu, X. W., et al., 2022. Co-Seismic Surface Deformation and Late Quaternary Accumulated Displacement along the Seismogenic Fault of the 2021 Madoi *M*7.4 Earthquake and Their Implications for Regional Tectonics. *Chinese Journal of Geophysics*, 65(8): 2984–3005. https://doi.org/10.6038/cjg2022P0873 (in Chinese with English Abstract)

Chen, W. K., Wang, D., Zhang, C., et al., 2022. Estimating Seismic Intensity Maps of the 2021 *M*w 7.3 Madoi, Qinghai and *M*w 6.1 Yangbi, Yunnan, China Earthquakes. *Journal of Earth Science*, 33(4): 839–846. https://doi.org/10.1007/s12583-021-1586-9

Chen, Z. Y., 2017. Mechanisms and Seismic Damage Control of Underground Large-Space Structures in Deep Soft Soil. Tongji University, Shanghai. March 20 (in Chinese)

Costantini, M., 1998. A Novel Phase Unwrapping Method Based on Network Programming. *IEEE Transactions on Geoscience and Remote Sensing*, 36(3): 813–821. https://doi.org/10.1109/36.673674

Deng, Q. D., Cheng, S. P., Ma, J., et al., 2014. Characteristics of Seismic Activity and Current Seismic Trends in the Qinghai-Tibet Plateau. *Chinese Journal of Geophysics*, 57(7): 2025–2042 (in Chinese with English Abstract)

Dou, J., Xiang, Z. L., Xu, Q., et al., 2023. Application and Development Trend of Machine Learning in Landslide Intelligent Disaster Prevention and Mitigation. *Earth Science*, 48(5): 1657–1674 (in Chinese with English Abstract)

Dou, J., Yunus, A. P., Merghadi, A., et al., 2020. Different Sampling Strategies for Predicting Landslide Susceptibilities are Deemed Less Consequential with Deep Learning. *Science of the Total Environment*, 720: 137320. https://doi. org/10.1016/j.scitotenv.2020.137320

Duman, T. Y., Emre, Ö., 2013. The East Anatolian Fault: Geometry, Segmentation and Jog Characteristics. *Geological Society, London, Special Publications*, 372(1): 495–529. https://doi.org/10.1144/sp372.14

Guo, Y. L., Li, H. F., Liang, P., et al., 2024. Preliminary Report of Coseismic Surface Rupture (Part) of Türkiye's *M*w7.8 Earthquake by Remote Sensing Interpretation. *Earthquake Research Advances*, 4(1): 100219. https://doi. org/10.1016/j.eqrea.2023.100219

Ha, G. H., Liu, J. R., Ren, Z. K., et al., 2022. The Interpretation of Seismogenic Fault of the Maduo *M*w 7.3 Earthquake, Qinghai Based on Remote Sensing Images—A Branch of the East Kunlun Fault System. *Journal of Earth Science*, 33(4): 857–868. https://doi.org/10.1007/s12583-021-1556-2

Huang, T., Wu, Z. H., Han, S., et al., 2024. Active Fault Characteristics and Potential Seismic Risk Assessment in Shigatse, Tibet. *Progress in Earthquake Science*, 54(10): 696–711. https://doi.org/10.19987/j.dzkxjz.2024-003 (in Chinese with English Abstract)

Institute of Geology, China Earthquake Administration, 2025. Preliminary Analysis of Crustal Deformation and Fault Models of the 2025 *M*s 6.8 Dingri Earthquake in Tibet. [2025-1-9]. https://www.eq-igl.ac.cn/zhxw/info/2025/38560.html (in Chinese)

Jara-Muñoz, J., Melnick, D., Li, S., et al., 2022. The Cryptic Seismic Potential of the Pichilemu Blind Fault in Chile Revealed by Off-Fault Geomorphology. *Nature Communications*, 13: 3371. https://doi.org/10.1038/s41467-022-30754-1

Kang, D. J., Chen, W. K., Zhao, H. Q., et al., 2023. Rapid

Assessment of the September 5, 2022 *M*s 6.8 Luding Earthquake in Sichuan, China. *Earthquake Research Advances*, 3(2): 100214. https://doi.org/10.1016/j.eqrea.2023.100214

Krüger, F., Ohrnberger, M., 2005. Tracking the Rupture of the *M*w = 9.3 Sumatra Earthquake over 1150 km at Teleseismic Distance. *Nature*, 435: 937–939. https://doi.org/10.1038/nature03696

Kusky, T., Bozkurt, E., Meng, J. N., et al., 2023. Twin Earthquakes Devastate Türkiye and Syria: First Report from the Epicenter: A Deadly Dance of the Plates: Arabia Takes a Step to the North, and Anatolia Jumps to the West. *Journal of Earth Science*, 34 (2): 291–296. https://doi.org/10.1007/s12583-023-1317-5

Li, Y. H., Cui, D. X., Hao, M., 2015. GPS-Constrained Inversion of Slip Rate on Major Active Faults in the Northeastern Margin of Tibet Plateau. *Earth Science*, 40(10): 1767 – 1780 (in Chinese with English Abstract)

Li, Y. S., Li, W. L., Xu, Q., et al., 2025. InSAR Coseismic Deformation Detection and Fault Slip Distribution Inversion of the Dingri Earthquake with *M*s 6.8 in Tibet on January 7, 2025. *Journal of Chengdu University of Technology* (*Science & Technology Edition*). Online first. 1 – 13. https://kns. cnki. net/kcms/detail/51.1634. N. 20250117.1150.002. html (in Chinese with English Abstract)

Liu, J., Chen, T., Zhang, P. Z., et al., 2013. Illuminating the Active Haiyuan Fault, China by Airborne Light Detection and Ranging. *Chinese Science Bulletin*, 58(1): 41–45 (in Chinese with English Abstract)

Lu, H. Y., Li, W. L., Xu, Q., et al., 2019. Early Detection of Landslides in the Upstream and Downstream Areas of the Baige Landslide, the Jinsha River Based on Optical Remote Sensing and InSAR Technologies. *Geomatics and Information Science of Wuhan University*, 44(9): 1342–1354 (in Chinese with English Abstract)

Lu, M. Y., Zhao, X. X., Wang, J. P., et al., 2024. Discussion and Analysis of Seismic Disaster Characteristics of the 6.2 Jishishan Earthquake in Gansu. *Progress in Earthquake Science*. Online first (in Chinese with English Abstract)

Mao, Z. J., Yu, H. Y., Liang, W., et al., 2024. Identification and Feature Analysis of Regional Loess Landslides Based on UAV Tilt Photogrammetry 3D Modeling. *Geology in China*, 51(2): 561–576 (in Chinese with English Abstract)

Mei, J. T., Wan, Y. G., 2024. Estimation of Coseismic Rupture Distribution of Twin Earthquakes in Türkiye Based on Priori Constraints and InSAR Data. *Earth Science*, 49(8): 2961 – 2978 (in Chinese with English Abstract)

Meng, J., Kusky, T., Mooney, W. D., et al., 2024. Surface Deformations of the 6 February 2023 Earthquake Sequence, Eastern Türkiye. *Science*, 383(6680): 298 – 305. https://doi. org/10.1126/science.adj3770

Nsangou Ngapna, M., Owona, S., Mvondo Owono, F., et al., 2018. Tectonics, Lithology and Climate Controls of Morphometric Parameters of the Edea-Eseka Region (SW Cameroon, Central Africa): Implications on Equatorial Rivers and Landforms. *Journal of African Earth Sciences*, 138: 219–232. https://doi.org/10.1016/j.jafrearsci.2017.11.008

Pan, Z. Y., He, J. K., Shao, Z. G., 2020. Spatial Variation in the Present-Day Stress Field and Tectonic Regime of Northeast Tibet from Moment Tensor Solutions of Local Earthquake Data. *Geophysical Journal International*, 221(1): 478 – 491. https://doi. org/10.1093/gji/ggaa013

Peng, L., Xu, S. N., Mei, J. J., et al., 2017. Recognition of Earthquake-Induced Landslides Using High-Resolution Remote Sensing Imagery. *Journal of Remote Sensing*, 21(4): 21 – 30 (in Chinese with English Abstract)

Sarma, J. N., Sharma, S., 2018. Neotectonic Activity of the Bomdila Fault in Northeastern India from Geomorphological Evidences Using Remote Sensing and GIS. *Journal of Earth System Science*, 127(8): 113. https://doi.org/10.1007/s12040-018-1008-2

Wan, Y. G., Shen, Z. K., Bürgmann, R., et al., 2017. Fault Geometry and Slip Distribution of the 2008 *M*w 7.9 Wenchuan, China Earthquake, Inferred from GPS and InSAR Measurements. *Geophysical Journal International*, 208(2): 748 – 766. https://doi. org/10.1093/gji/ggw421

Wang, F. C., 2023. Factors and Prediction Models of Seismic Ground Motion Topographic Effects: [Dissertation]. Institute of Engineering Mechanics, China Earthquake Administration, Beijing (in Chinese with English Abstract)

Wang, S. H., Ai, M., Wu, C. Y., et al., 2018. Application of High-Resolution Satellite Imagery-Derived DEM in Quantitative Research of Active Tectonics: A Case Study of the Southern Margin Fault of the Kumishi Basin. *Seismology and Geology*, 40 (5): 999–1017(in Chinese with English Abstract)

Wang, Y. P., Shen, J., Song, Y. J., et al., 2017. Interpretation of Fault Characteristics in Funiu Mountains, Western Henan Based on ASTER GDEM. *China Earthquake Engineering Journal*, 39(4): 767–773. https://doi.org/10.3969/j.issn.1000-0844.2017.04.0767 (in Chinese with English Abstract)

Wang, Y., Zhang, B., Hou, J. J., et al., 2014. Structure and Tectonic Geomorphology of the Qujiang Fault at the Intersection of the Ailao Shan-Red River Fault and the Xianshuihe-Xiaojiang Fault System, China. *Tectonophysics*, 634: 156 – 170. https://doi. org/10.1016/j.tecto.2014.07.031

Wu, Z. H., Long, C. X., Fan, T. Y., et al., 2015. Arc-Twisting Tectonic Systems and Their Dynamic Characteristics in the Southeastern Qinghai-Tibet Plateau. *Geological Bulletin of China*, 34(1): 1–31 (in Chinese with English Abstract)

Xing, K., Li, H., Zhang L. L., et al., 2025. Analysis of Surface Rupture and Seismic Damage Characteristics of the January 7, 2025, Dingri *M*s6.8 Earthquake in Xizang. *Safety and Environmental Engineering*, Online First. https://doi. org/10.13578/j. cnki. issn.1671-1556.20250133.

Xu, Q., 2020. Insights and Thoughts on the Early Identification of Geological Disaster Hazards. *Journal of Wuhan University* (*Information Science Edition*), 45(11): 1651 – 1659 (in Chinese with English Abstract)

Xu, Q., Dong, X. J., Li, W. L., et al., 2019. Early Identification and Monitoring and Warning of Major Geological Disaster Hazards Based on Air-Space-Ground Integrated Systems. *Journal of Wuhan University* (*Information Science Edition*), 44(7): 957–966 (in Chinese with English Abstract)

Yang, Y. C., Dou, J., Merghadi, A., et al., 2024. Advanced Prediction of Landslide Deformation through Temporal Fusion Transformer and Multivariate Time-Series Clustering of InSAR: Insights from the Badui Region, Eastern Tibet. *IEEE Transactions on Geoscience and Remote Sensing*, 62: 4514219. https://doi.org/10.1109/TGRS.2024.3504241

You, Z. C., Bi, H. Y., Zheng, W. J., et al., 2023. Fine Characteristic Study of Earthquake Rupture Zone Based on High-Resolution

Remote Sensing Imagery: A Case Study of the Litang Fault. *Seismology and Geology*, 45(5): 1057 – 1073. https://doi. org/10.3969/j. issn. 0253-4967.2023.05.002 (in Chinese with English Abstract)

Yu, J. C., Li, S. W., Yuan, D. Y., et al., 2025. Late Quaternary Tectonic Deformation and Earthquake Mechanism of Xinminbao Fault Revealed by UAV Photogrammetry. *Earth Scienc*e. Online first. 1–16 (in Chinese with English Abstract)

Zhang, C. L., Li, Z. H., Zhang, S. C., et al., 2022. Comprehensive Remote Sensing Interpretation of the 2022 *M*w6.7 Menyuan, Qinghai Earthquake Surface Rupture Zone. *Journal of Wuhan University* (*Information Science Edition*), 47(8): 1257 – 1270 (in Chinese with English Abstract)

Zhang, J. J., Guo, L., Ding, L., et al., 2002. Structural Characteristics of the Middle and Southern Segments of the Shenzha-Dingjie Normal Fault System and Their Relationship with the South Tibetan Detachment System. *Chinese Science Bulletin*, 47(10): 738–743 (in Chinese with English Abstract)

Zhang, J. L., Gong, Q. Z., 2024. Analysis of Seismic Tectonic Features in Tibet Autonomous Region. *Tibet Science and Technology*, 46(12): 13–18+40 (in Chinese with English Abstract)

Zhang, L. L., Zhang, R. Q., Dou, J., et al., 2025. Advancing Reservoir Landslide Stability Assessment *via* TS-InSAR and Airborne LiDAR Observations in the Daping Landslide Group, Three Gorges Reservoir Area, China. *Landslides*, 22(1): 169 – 188. https://doi.org/10.1007/s10346-024-02337-2

Zhou, Y., Parsons, B., Elliott, J. R., et al., 2015. Assessing the Ability of Pleiades Stereo Imagery to Determine Height Changes in Earthquakes: A Case Study for the El Mayor-Cucapah Epicentral Area. *Journal of Geophysical Research*: *Solid Earth*, 120(12): 8793–8808. https://doi.org/10.1002/2015jb012358

Zhu, J. J., Li, Z. W., Hu, J., 2017. Research Progress and Methods of InSAR for Deformation Monitoring. *Acta Geodaetica et Cartographica Sinica*, 46(10): 1717–1733. https://doi.org/10.11947/j. AGCS. 2017.20170350 (in Chinese with English Abstract)